FRONTIERS OF PHYSICS

RESEARCH ARTICLE
Volume 20 / Issue 2 / 025202 / 2025

Holographic einstein ring of deformed AdS-Schwarzschild black holes

Jin-Yu Gui[1], Ke-Jian He[1], Huan Ye[2], Xiao-Xiong Zeng[3,†]

1 Department of Mechanics, Chongqing Jiaotong University, Chongqing 400074, China
2 School of Materials Science and Engineering, Chongqing Jiaotong University, Chongqing 400074, China
3 College of Physics and Electronic Engineering, Chongqing Normal University, Chongqing 401331, China
Corresponding author. E-mail: †xxzengphysics@163.com
Received July 5, 2024; accepted November 20, 2024

ABSTRACT

In this work, the wave optics is employed to investigate the Einstein ring of a deformed AdS-Schwarzschild black hole (BH). When the source is fixed on the AdS boundary, one can obtain the corresponding response function generated on the antipodal side of the boundary. By utilizing a virtual optical system equipped with a convex lens, we are able to capture an image of the BH's holographic Einstein ring on the screen. The influence of the relevant physical parameters and the observer's position on the characteristics of the Einstein ring is also investigated, revealing that variations in the observer's position result in a transition of the displayed image from an axisymmetric ring to an arc, ultimately converging into a solitary point of luminosity. In addition, variations in the relevant physical parameters naturally exert influences on the Einstein ring. The photon ring of the BH was also investigated from a geometric optics perspective, and the numerical results indicate that the incident angle of the photon ring aligns with that of the Einstein ring. In the context of modified gravity theories, the investigation of Einstein rings formed by deformed AdS-Schwarzschild BH is expected to not only contribute to advancing the development of gravitational theories but also facilitate a more comprehensive understanding of spacetime geometry and the physical properties of BHs, thereby distinguishing them from Schwarzschild BH.

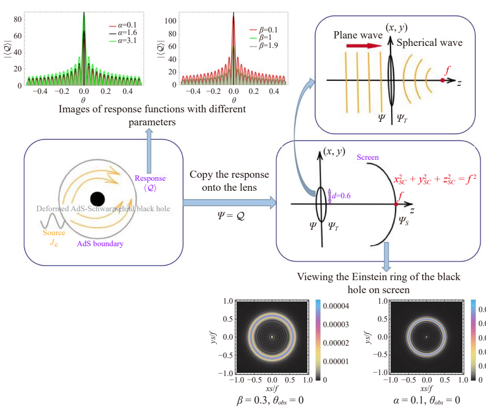

Keywords deformed AdS-Schwarzschild black hole, AdS/CFT correspondence, Einstein ring, wave optics

1 Introduction

The AdS/CFT correspondence [1], also known as holographic duality or gauge/gravity duality, establishes a profound connection between classical gravitational theory in Anti-de Sitter (AdS) spacetime and quantum field theories (QFTs). Due to its particularity, it has been a focal point of research for numerous physicists over the past few decades and serves as a bridge spanning different disciplinary fields [2]. The relevant research in the field of holographic duality not only serves to test the internal consistency of the theory, but also provides a novel platform for advancing the study of strongly coupled field theory. The concept of holographic duality has been extensively utilized in the investigation of holographic superconductivity [3–5], Fermi and non-Fermi liquids [6–8], exotic metals [9–11] and Metal insulation phase transition in quantum phase transition [12–14].

The black hole (BH) shadow, being an observable characteristic of a BH, has consistently remained a prominent subject in the realms of theoretical physics and astronomy. The Event Horizon Telescope (EHT) project successfully captured images of BH shadows located at the center of both the M87 galaxy and our Milky Way [15, 16], marking a significant milestone in astronomical observations. Currently, the study of BH shadows is extensive in various spacetime, including binary BH shadows [17], different configurations of BHs [18–24], dynamically evolving spacetimes [25], wormholes [26–28], and naked singularities [29]. The presence of a luminous ring positioned beyond the event horizon of BHs has been demonstrated through images and associated research. The ring structure, resulting from the extensive accumulation of high-energy matter surrounding the BH, is commonly referred to as the photon ring. Not only does the photon ring serve as a valuable tool for testing general relativity (GR), but it also provides crucial insights into the structural composition of spacetime.

The current research on BH shadows primarily relies on geometric optics, focusing on the behavior of photons in close proximity to BHs. Recently, Hashimoto *et al.* [30] employed wave optics to investigate the shadows cast by BHs, presenting a captivating and innovative approach. Especially in Ref. [31], a significant breakthrough was made concerning the existence of a sequence of luminous ring structures, known as Einstein rings, which encircling the AdS Schwarzschild BH based on the principle of holographic duality. It has been observed that holographic images of the BH, which result from its gravitational lensing effect, can be constructed using the response function for a thermal state on a two-dimensional sphere which is dual to the Schwarzschild-AdS BH. Furthermore, clear observation of Einstein rings is possible. This methodology has also been employed in holographic superconductivity models [32], wherein researchers have unveiled a discontinuous alteration in the size of the photon ring. The charged BHs [33] have also been studied accordingly, and the result showed that the chemical potential has no influence on the radius of the Einstein ring, and the temperature dependence of the Einstein ring exhibits a unique characteristic. In the context of other modified gravity theory, the study of holographic Einstein rings of BHs has yielded some interesting results, which can be found in Refs. [34–41].

The AdS-Schwarzschild BH, being a classical solution in the AdS spacetime, has been extensively investigated due to its profound insights into the nature of BHs, gravity, and the universe's structure within the AdS framework [42–46]. In the context of modified gravity theories, studies on AdS-Schwarzschild BHs, including investigations of deformed solutions, are also of paramount importance. In the work [47], the author obtained deformed AdS-Schwarzschild BH solutions using the gravity decoupling (GD) method, which extends known solutions of the standard gravitational action to additional sources and modified theories of gravitation. Furthermore, the effects of deformation parameters on the horizon structure, thermodynamics and Hawking-Page phase transition temperature are also studied. However, the shadow of the deformed AdS-Schwarzschild BH remains unexplored.

However, the holographic Einstein rings associated with deformed ADS-Schwarzschild BHs remains uncharted territory, constituting the focal point of this paper. In this study, we aim to investigate the Einstein rings of the deformed AdS-Schwarzschild BH using wave optics, based on the AdS/CFT correspondence, and explore the impact of relevant physical parameters on the Einstein rings.

The paper is organized as follows. In Section 2, we briefly introduce the deformed AdS-Schwarzschild BH and derive the lensing response function that describes the diffraction of a wave source by the BH in this spacetime background. In Section 3, we employ an optical system equipped with a convex lens to observe the Einstein ring formed on the screen. We pay particular attention to the influence of the relevant physical parameters and the observer's position on the Einstein ring. Furthermore, we compare the relevant conclusions obtained through wave optics with those derived from geometric optics. Finally, in Section 4, we summarize the key findings and conclusions of our study.

2 The deformed AdS-Schwarzschild BH and its response function

We consider the BH solution of a deformed AdS-Schwarzschild BH with the following metric [46]

$$\mathrm{d}s^2 = -F(r)\mathrm{d}t^2 + \frac{1}{F(r)}\mathrm{d}r^2 + r^2(\mathrm{d}\theta^2 + \sin^2\theta\mathrm{d}\varphi^2), \quad (1)$$

with

$$F(r) = 1 - \frac{2M}{r} + \frac{r^2}{\tilde{l}^2} + \alpha\frac{\beta^2 + 3r^2 + 3\beta r}{3r(\beta + r)^3}. \quad (2)$$

The parameter α, known as the deformation parameter, modulates the influence of geometric deformations on the background geometry by adjusting their intensity, while M represents the ADM mass of the BH. In addition, the term β is a control parameter with a length dimension that serves to prevent the occurrence of the central singularity. $\tilde{l} = \sqrt{3/|\Lambda|}$ is the AdS radius, where Λ is the cosmological constant. In what follows, the value of $\tilde{l}$ is taken as $\tilde{l} = 1$ for the purpose of simplifying calculations. Substituting the metric function mentioned above with the variable $r = 1/y$ and $G(y) = F(1/r)$, Eq. (1) can be written as

$$\mathrm{d}s^2=\frac{1}{y^2}\left[-G(y)\mathrm{d}t^2+\frac{\mathrm{d}y^2}{G(y)}+\mathrm{d}\theta^2+\sin^2\theta\mathrm{d}\varphi^2\right],\quad(3)$$

$$G(y)=1+y^2-2My^3+\frac{y^3\alpha\left(\frac{3}{y^2}+\frac{3\beta}{y}+\beta^2\right)}{3\left(\frac{1}{y}+\beta\right)^3}.\quad(4)$$

At $y=\infty$, a space-time singularity emerges, while at $y=0$, the corresponding system resides on the AdS boundary. Note that the temperature of the BH is defined by the Hawking temperature, which is given by the relation $T=\frac{1}{4\pi}G'(y_h)$, where $y=y_h$ represents the event horizon of the BH.

Next, we consider the dynamics of a massless scalar field based on the following Klein–Gordon equation [31]

$$D_aD^a\tilde{\Psi}=0.\quad(5)$$

In order to solve the Klein–Gordon equation more conveniently, we use the incident Eddington–Finkelstein coordinate system [33], which facilitates our observation of the BH's nature and ensures the continuity of physical quantities at the event horizon. The coordinates can be expressed as

$$\upsilon\equiv t+y_*=t-\int\frac{\mathrm{d}y}{G(y)},\quad(6)$$

hence, the metric function in Eq. (3) can be expressed as follows:

$$\mathrm{d}s^2=\frac{1}{y^2}\Big[-G(y)\mathrm{d}\upsilon^2-2\mathrm{d}y\mathrm{d}\upsilon+\mathrm{d}\theta^2+\sin^2\theta\mathrm{d}\varphi^2\Big].\quad(7)$$

Near the AdS boundary, the asymptotic solution of the scalar field is

$$\begin{aligned}\tilde{\Psi}(\upsilon,y,\theta,\varphi)=&J_{\mathcal{Q}}(\upsilon,\theta,\varphi)+y\partial_\upsilon J_{\mathcal{Q}}(\upsilon,\theta,\varphi)\\&+\frac{1}{2}y^2D_S^2J_{\mathcal{Q}}(\upsilon,\theta,\varphi)+\langle\mathcal{Q}\rangle y^3+Q(y^4),\end{aligned}\quad(8)$$

where D_S^2 denotes the scalar Laplacian on the unit S^2. Based on the AdS/CFT framework, $J_{\mathcal{Q}}$ can be interpreted as the material source on the boundary [48]. We select a monochromatic and axisymmetric Gaussian wave packet as the wave source, located at the South pole ($\theta_0=\pi$) of the AdS boundary, as shown in Fig. 1:

$$\begin{aligned}J_{\mathcal{Q}}(\upsilon,\theta)&=\mathrm{e}^{-\mathrm{i}\omega\upsilon}(2\pi\eta^2)^{-1}\exp\left[-\frac{(\pi-\theta)^2}{2\eta^2}\right]\\&=\mathrm{e}^{-\mathrm{i}\omega\upsilon}\sum_{l=0}^{\infty}C_{l0}X_{l0}(\theta),\end{aligned}\quad(9)$$

where η denotes the width of the wave generated by the Gaussian source, and $\eta\ll\pi$. The parameter ω represents the frequency of the incident wave. $X_{l0}(\theta)$ is the spherical harmonics function, and C_{l0} is the coefficients of $X_{l0}(\theta)$, which can be expanded as

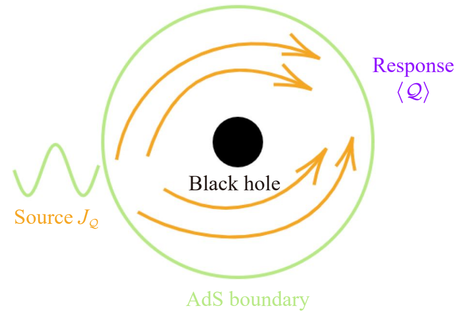

Fig. 1 Diagram of the response function and the source.

$$C_{l0}=(-1)^l\sqrt{\frac{l+1/2}{2\pi}}\exp\left[-\frac{(l+1/2)^2\eta^2}{2}\right].\quad(10)$$

Then, considering the symmetry of spacetime, the scalar field $\tilde{\Psi}(\upsilon,y,\theta,\varphi)$ can be decomposed into

$$\tilde{\Psi}(\upsilon,y,\theta,\varphi)=\sum_{l=0}^{\infty}\sum_{n=-l}^{l}\mathrm{e}^{-\mathrm{i}\omega\upsilon}C_{l0}Y_l(y)X_{ln}(\theta,\varphi).\quad(11)$$

The corresponding response function $\langle\mathcal{Q}\rangle$ can be expanded as

$$\langle\mathcal{Q}\rangle=\sum_{l=0}^{\infty}\mathrm{e}^{-\mathrm{i}\omega\upsilon}C_{l0}(\mathcal{Q})_lX_{l0}(\theta).\quad(12)$$

In Eq. (11), the radial wave function Y_l satisfies the equation of motion as follows:

$$\begin{aligned}&y^2G(y)Y_l''+(y^2G'(y)-2yG(y)+2\mathrm{i}\omega y^2)Y_l'\\&\quad+[-2\mathrm{i}\omega y-y^2l(l+1)]Y_l=0.\end{aligned}\quad(13)$$

According to the AdS/CFT correspondence, near the AdS boundary Y_l can be expanded as

$$\lim_{y\to0}Y_l=1-\mathrm{i}\omega y+\frac{y^2(-l(1+l))}{2}+\langle\mathcal{Q}\rangle_l\,y^3+Q(y^4).\quad(14)$$

Obviously, the function Y_l has two boundary conditions, one of which is at the event horizon $y=y_h$, and has the following form

$$(y_h^2G'+2\mathrm{i}\omega y_h^2)Y_l'-[2\mathrm{i}\omega y_h+y_h^2l(l+1)]Y_l=0.\quad(15)$$

The other is at $y=0$, namely the AdS boundary. In this case, the wave source $J_{\mathcal{Q}}$ is the asymptotic form of the scalar field at infinity, and $Y_l(0)=1$, which can be seen from Eq. (13). We get the corresponding numerical solution of Y_l, and extract $\langle\mathcal{Q}\rangle_l$ by using the pseudo-spectral method [30, 31]. Subsequently, using Eq. (12) to get the value of the total response function. In

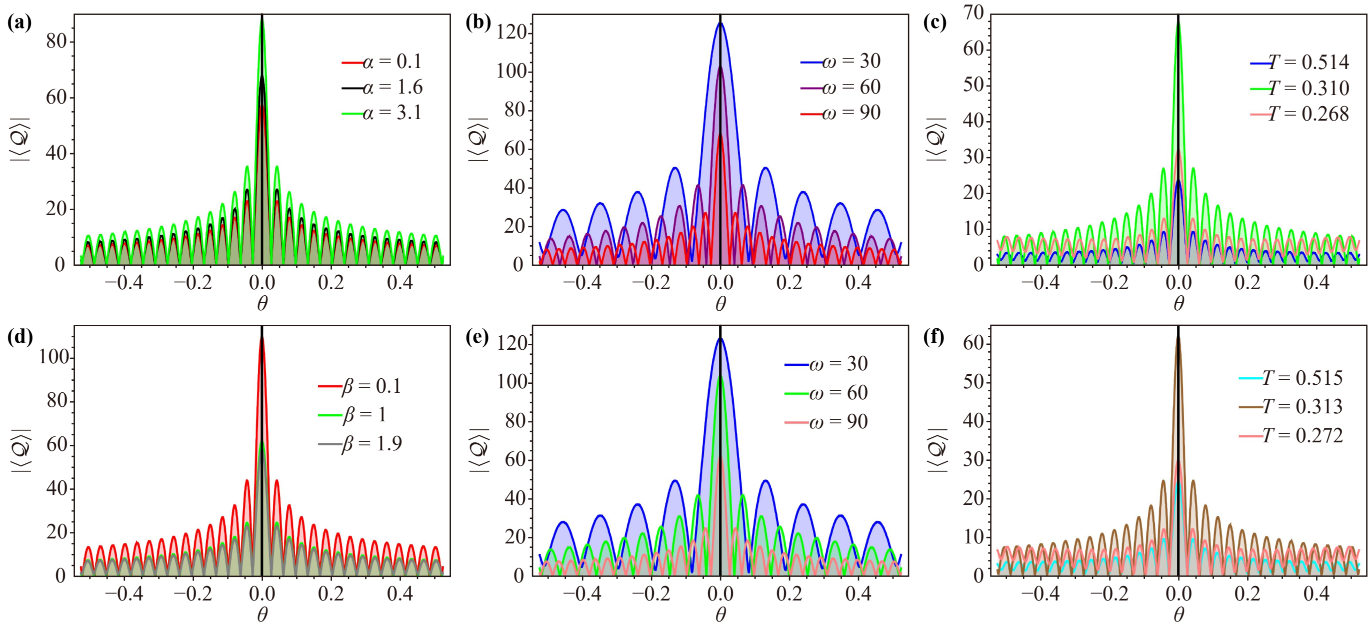

Fig. 2 **(a)** Effect of different α on the response function, where $\beta=1$, $y_h=1$, $\omega=90$. **(b)** Effect of different ω on the response function, where $\alpha=1.6$, $y_h=1$, $\beta=1$. **(c)** Effect of different T on the response function, where $\alpha=1.6$, $\beta=1$, $\omega=90$. **(d)** Effect of different β on the response function, where $\alpha=1$, $y_h=1$, $\omega=90$. **(e)** Effect of different ω on the response function, where $\alpha=1$, $y_h=1$, $\beta=1$. **(f)** Effect of different T on the response function, where $\alpha=1$, $\beta=1$, $\omega=90$.

Figs. 2(a)–(c), fixing the control parameter β at 1 and varying the deformation parameter α and other parameters to observe the amplitude of the response function. It can be observed from Fig. 2(a) that the amplitude of the response function increases with the increase of the deformation parameter α. Meanwhile, Fig. 2(b) indicates that the period of the response function decreases with the increase of the wave source frequency ω. As can be seen from Fig. 2(c), the amplitude of the response function exhibits a notable variation with temperature, yet the relationship is not linear. For instance, at $T=0.310$, the amplitude of the response function attains its peak, and subsequently diminishes at $T=0.268$ and $T=0.514$.

For simplicity and without loss of generality, we fix the deformation parameter $\alpha=1$ and change the control parameter β and other parameters, as shown in Figs. 2(d)–(f). The amplitude of the response function decreases with the increase of the control parameter β and the wave source frequency ω, as shown in Figs. 2(d) and (e), respectively. In Fig. 2(f), the amplitude of the response function reached its maximum when $T=0.313$ and decreased smoothly when $T=0.272$ and $T=0.515$.

3 The formation of holographic ring

Although the response function has been derived, it does not exhibit holographic image. To achieve this goal, it is necessary to incorporate an optical setup equipped with a convex lens. The convex lens converts a plane wave into a spherical wave, and the angle observed at the AdS boundary is θ_{obs}. A new coordinate (θ',φ') is obtained by rotating coordinate (θ,φ), and the following relation is satisfied [33]:

$$\cos\varphi' + \mathrm{i}\cos\theta' = \mathrm{e}^{\mathrm{i}\theta_{obs}}(\sin\theta\cos\varphi + \mathrm{i}\cos\theta), \tag{16}$$

where $\theta'=0,\varphi'=0$ correspond to the observational center. A Cartesian coordinate system (x,y,z) is established such that $(x,y)=(\theta'\cos\varphi',\theta'\sin\varphi')$ at the boundary where the observer located, for a virtual optical system. The convex lens is adjusted on a two-dimensional plane (x,y), in which the focal length of the lens and corresponding radius are denoted by f and d, respectively. Further, the coordinates on the spherical screen are defined as $(x,y,z)=(x_{SC},y_{SC},z_{SC})$, satisfying $x_{SC}^2+y_{SC}^2+z_{SC}^2=f^2$. The relationship between the incident wave $\Psi(\tilde{x})$ before passing through the convex lens and the outgoing wave $\Psi_T(\tilde{x})$ after passing through the convex lens satisfies

$$\Psi_T(\tilde{x}) = \mathrm{e}^{-\mathrm{i}\omega\frac{|\tilde{x}|^2}{2f}}\Psi(\tilde{x}). \tag{17}$$

The wave function on the screen can be represented as [33]

$$\begin{aligned}\Psi_{SC}(\tilde{x}_{SC}) &= \int_{|\tilde{x}|\le d} \mathrm{d}^2x\Psi_T(\tilde{x})\mathrm{e}^{\mathrm{i}\omega R}\\ &\propto \int_{|\tilde{x}|\le d} \mathrm{d}^2x\Psi(\tilde{x})\mathrm{e}^{-\mathrm{i}\frac{\omega}{f}\tilde{x}\cdot\tilde{x}_{SC}}\\ &= \int \mathrm{d}^2x\Psi(\tilde{x})\sigma(\tilde{x})\mathrm{e}^{-\mathrm{i}\frac{\omega}{f}\cdot\tilde{x}\cdot\tilde{x}_{SC}},\end{aligned} \tag{18}$$

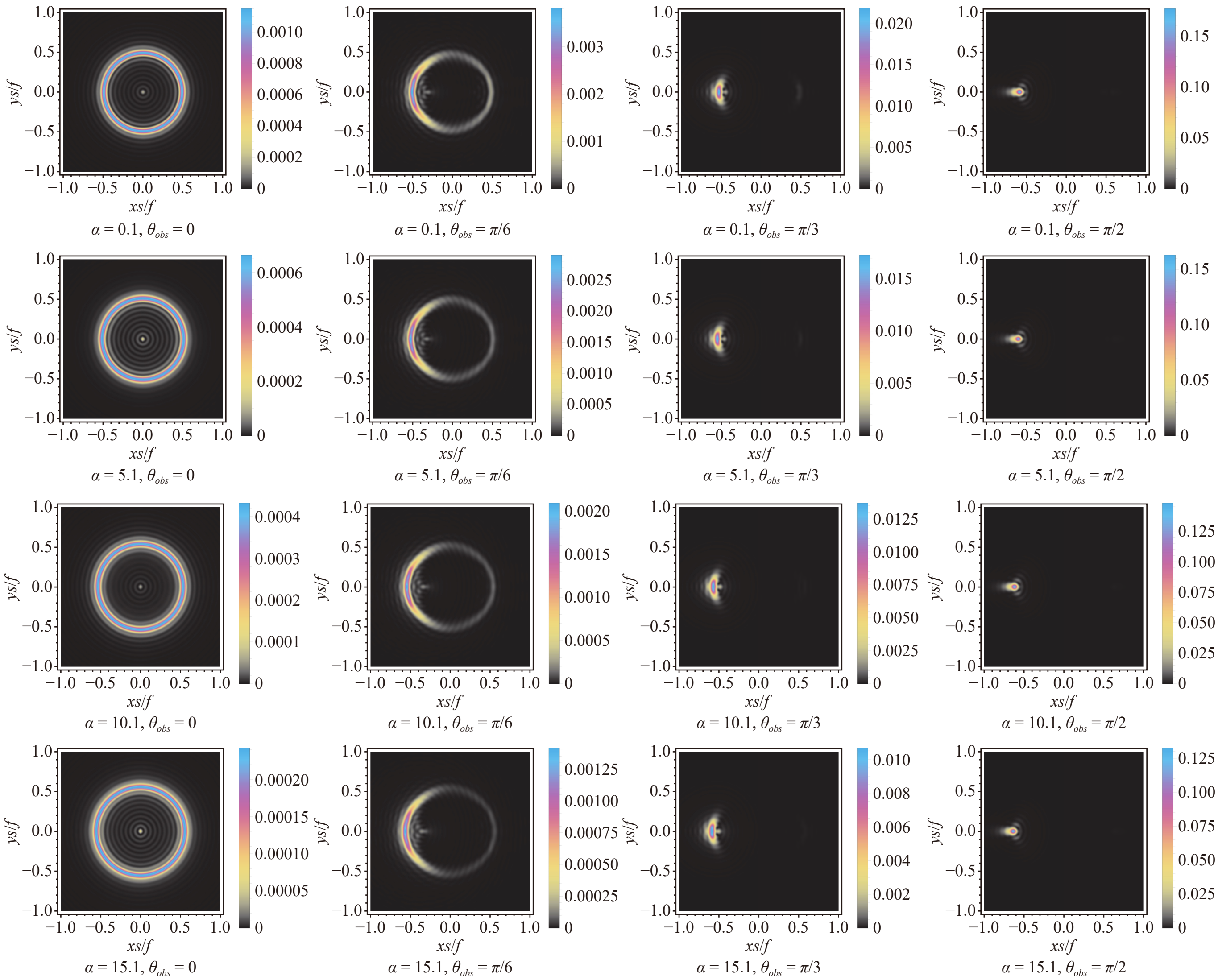

Fig. 3 Observational appearance of the response on the screen for different α at various observation angles, where $y_h = 5$, $\omega = 90$.

where R is the distance from the point $(x, y, 0)$ on the lens to the point $(x_{SC}^2, y_{SC}^2, z_{SC}^2)$ on the screen. In the formula, $\sigma(\tilde{x})$ is the window function, which is defined as

$$\sigma(\tilde{x}) := \begin{cases} 1, & 0 \le |\tilde{x}| \le d; \\ 0, & |\tilde{x}| > d. \end{cases} \tag{19}$$

From Eq. (18), it is evident that the observed wave on the screen is associated with the incident wave through the Fourier transform. In this article, the response function is considered as the incident wave $\Psi(\tilde{x})$, and we can observe the holographic images on this screen, using Eq. (18). The effects of the deformation parameter α, control parameter β, and Gaussian wave source on holographic images are investigated, with the source width $\eta = 0.02$ and radius of convex lens $d = 0.6$.

3.1 The effect of deformation parameter α on the images

Initially, holographic images obtained by varying the deformation parameter α and the observer's position θ_{obs} are presented in Fig. 3. When $\theta_{obs} = 0$, it indicates that the wave source is fixed at the south pole of the AdS boundary, while the observer is situated at the north pole, observing a series of axisymmetric concentric rings. As $\theta_{obs} = \pi/6$ (see the second column), the holographic ring transitions from strict spherical symmetry to axisymmetry, accompanied by a decrease in brightness. As it increases to $\theta_{obs} = \pi/3$ and $\theta_{obs} = \pi/2$, the holographic ring gradually disappears, especially at $\theta_{obs} = \pi/2$ where only bright spots are visible. This demonstrates that the shape of the holographic ring strongly depends on the observer's position. In the leftmost column of Fig. 3, despite variations in the value of α, a brightest circular

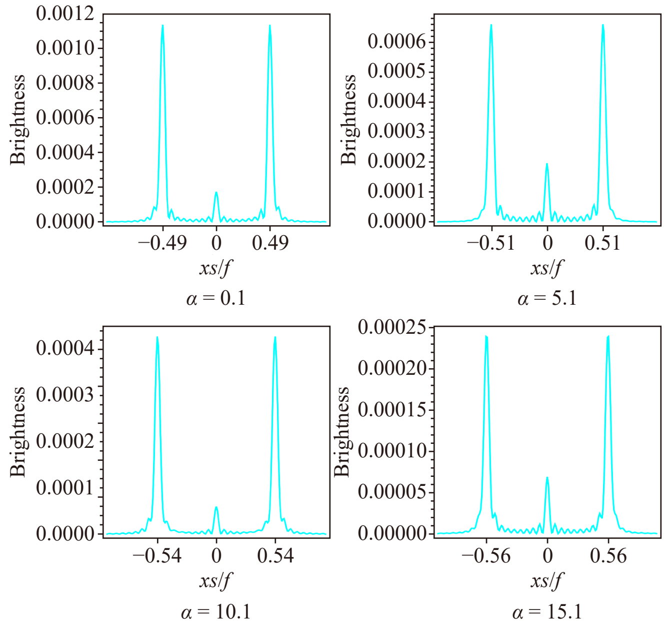

Fig. 4 Effect of α on the brightness, where $\theta_{obs}=0$, $y_h=5$, $\omega=90$.

ring persists, known as the Einstein ring. In addition, to further investigate the impact of the deformation parameter α on the Einstein ring, the brightness is plotted in Fig. 4, in which the distance between the two peak trajectories corresponds to the diameter of the Einstein ring. The increase in α results in a gradual increase in the radius of the Einstein ring. When $\alpha=0.1$, the radius of the ring is 0.49, and when $\alpha=15.1$, the radius of the ring is 0.56. Furthermore, the luminosity represented on the y-axis of Fig. 4 gradually decreases as α increases.

Next, the impact of the event horizon on the Einstein ring of BH is investigated. For simplicity, only the case

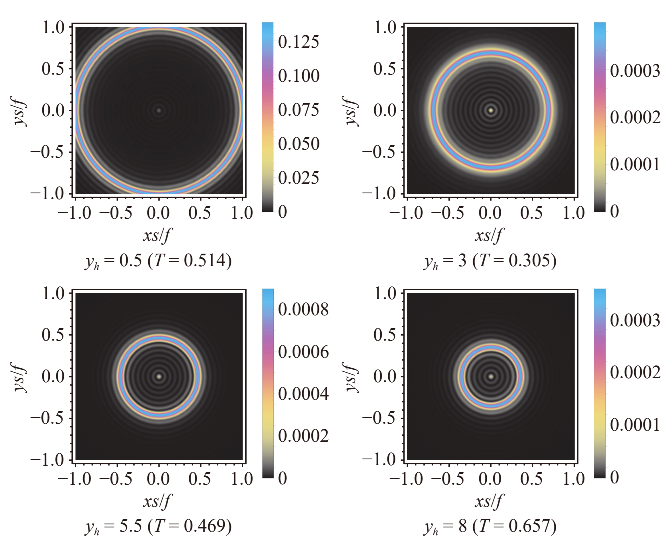

Fig. 5 Effect of y_h on the Einstein ring, where $\theta_{obs}=0$, $\alpha=1.6$, $\omega=90$.

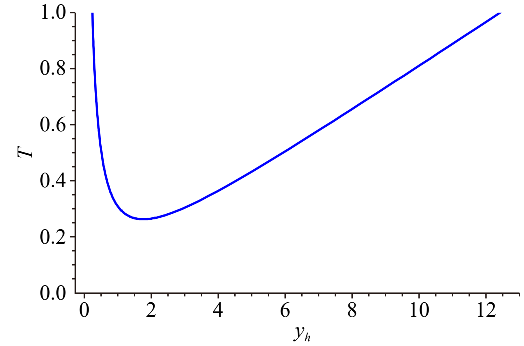

Fig. 6 The relationship between temperature and event horizon y_h, where $\alpha=1.6$, $\beta=1$.

where $\theta_{obs}=0$ is considered, as depicted in Fig. 5. When $y_h=0.5$, a bright spherically symmetric ring appears on the screen. Additionally, as y_h increases from 0.5 to higher values, such as $y_h=3$ and $y_h=5.5$, the ring gradually contracts. Notably, when $y_h=8$, the ring radius reaches its minimum. The observation indicates that as y_h increases, the ring radius decreases. However, there is no apparent pattern of change in the ring radius with temperature. In Ref. [33], the authors discussed the variation of ring radius with temperature. Here we argue that the variation of ring radius with the event horizon radius is more reasonable, as the relationship between the BH temperature and the event horizon is not monotonic, as depicted in Fig. 6.

Similarly, Fig. 7 depicts the relationship between luminosity and the event horizon. When $y_h=0.5$, $xs/f=1$, the luminosity is maximum. With increasing

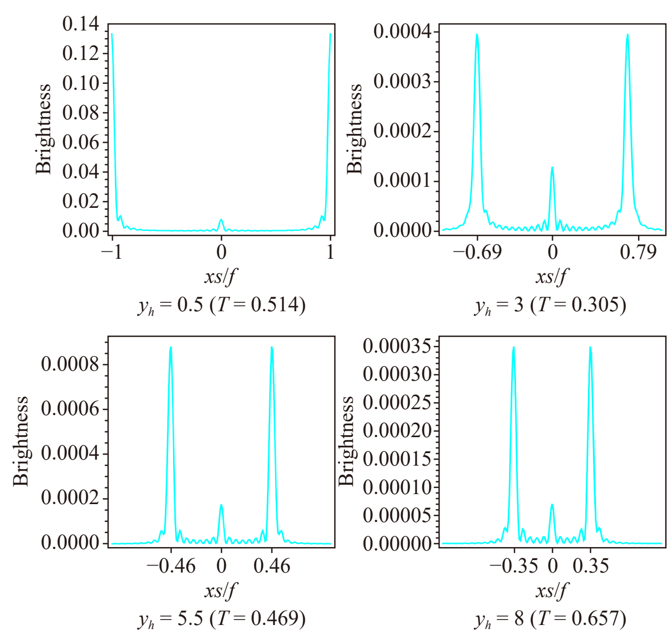

Fig. 7 Effect of T on the brightness, where $\theta_{obs}=0$, $\alpha=1.6$, $\omega=90$.

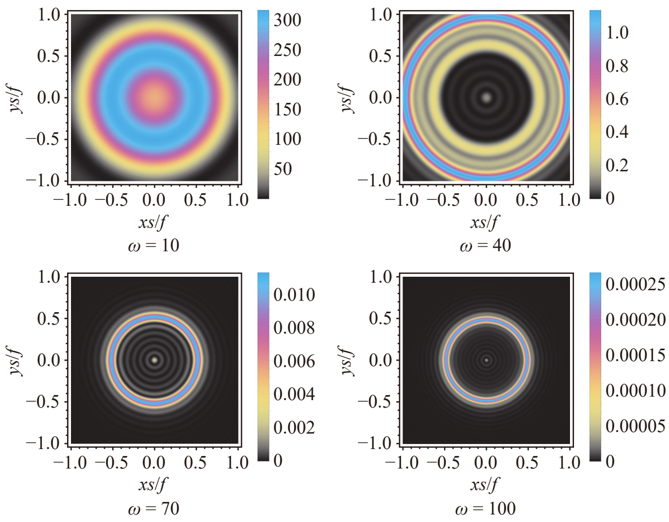

Fig. 8 Effect of ω on the Einstein ring, where $\theta_{obs}=0$, $\alpha=1.6$, $y_h=5$.

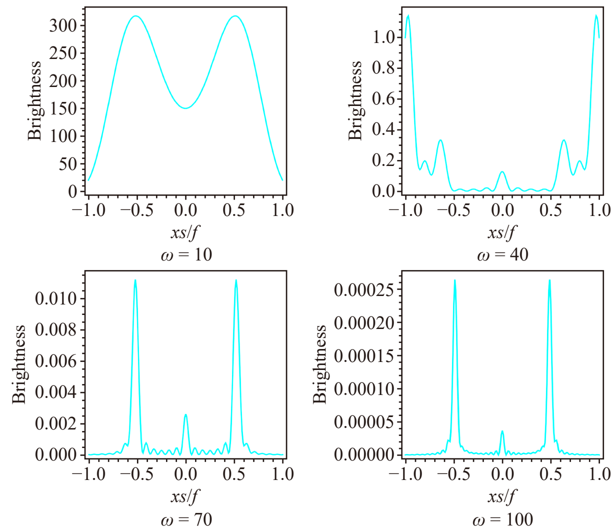

Fig. 9 Effect of ω on the brightness, where $\theta_{obs}=0$, $\alpha=1.6$, $y_h=5$.

y_h, the value of xs/f corresponding to the maximum luminosity decreases, indicating a decreases in the Einstein ring's radius.

The impact of wave sources, such as the wave source frequency ω, on the Einstein ring can also be analyzed. As demonstrated in Fig. 8, a discernible trend emerges where the resolution of the Einstein ring improves as the wave source frequency increases. At $\omega=40$, multiple diffraction rings are observable, indicating significant interference effects. However, as the frequency rises to $\omega=100$, these additional diffraction rings gradually fade, leaving only the primary Einstein ring distinct. This transition can be attributed to the increasing dominance of geometric optics at higher frequencies. To complement our understanding of these findings, Fig. 9 depicts the correlation between luminosity and angular frequency in Fig. 9. It is evident that high frequencies are crucial for effectively observing and resolving the radius of the ring.

3.2 The effect of control parameter β on the images

Similarly, as the control parameter β changes, a series of concentric rings can be observed in the leftmost column of Fig. 10. As the observer's position θ_{obs} varies from $\theta_{obs}=0$ to $\theta_{obs}=\pi/2$, the Einstein ring transitions from strict spherical symmetry to axial symmetry, accompanied by a decrease in partial brightness. Subsequently, the ring gradually diminishes, ultimately leaving only a single light spot. Figure 11 indicates that the radius of the Einstein ring gradually decreases as β increases. Specifically, when $\beta=0.3$, the radius of the ring is 0.6, and when $\beta=0.75$, the radius of the ring decreases to 0.5. Furthermore, as β increases, the luminosity gradually intensifies.

In Fig. 12, we analyze the impact of the event horizon on the Einstein ring of a BH. The results reveal a reciprocal relationship as y_h increases, the radius of the ring decreases correspondingly. Figure 13 illustrates the relationship between luminosity and the radius of the event horizon. As y_h gradually increases, the horizontal coordinate corresponding to the maximum luminosity gradually decreases, indicating that the radius of the Einstein ring diminishes with the increase of y_h.

3.3 Images from the viewpoint of geometric optics

In this section, we will discuss Einstein rings from the perspective of geometric optics. Our primary focus is on studying the incidence angle of photons, based on the spherically symmetric spacetime background described in Eq. (1) and Eq. (2). We define conserved quantities within the metric framework as $\omega=G(r)\partial t/\partial\lambda$ and $\tilde{L}=r^2\partial\varphi/\partial t$, where ω represents the energy of the photon, $\tilde{L}$ denotes the angular momentum of the photon and λ is the affine parameter. Due to the spherical symmetry of spacetime, it is only necessary to consider the case where photon orbits are located at the equator. $\theta\equiv\pi/2$. The four-velocity $\upsilon^{\varsigma}=(\mathrm{d}/\mathrm{d}\lambda)^{\varsigma}$ is satisfied

$$-G(r)(\mathrm{d}t/\mathrm{d}\lambda)^2+G(r)^{-1}(\mathrm{d}r/\mathrm{d}\lambda)^2 + r^2\sin\theta(\mathrm{d}\varphi/\mathrm{d}\lambda)^2=0, \tag{20}$$

and

$$\dot{r}^2=\omega-\tilde{L}z(r). \tag{21}$$

here $z(r)=G(r)/r^2$ and $\dot{r}=\partial r/\partial\lambda$. The incident angle $n^{\varsigma}\equiv\partial/\partial r^{\varsigma}$ with boundary θ_{in} as normal vector is defined as [33, 35]

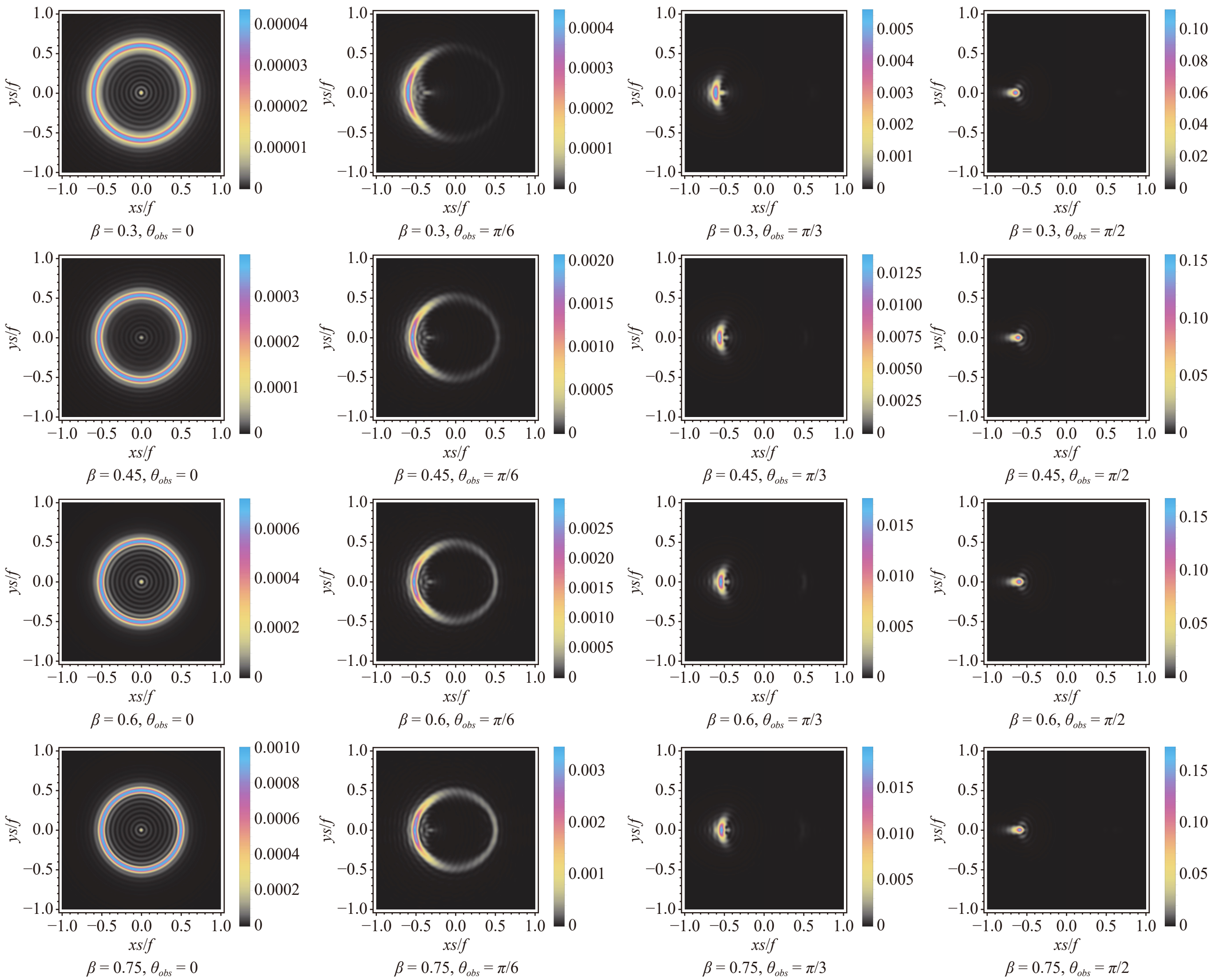

Fig. 10 Observational appearance of the response on the screen for different β at various observation angles, where $y_h = 5$, $\omega = 90$.

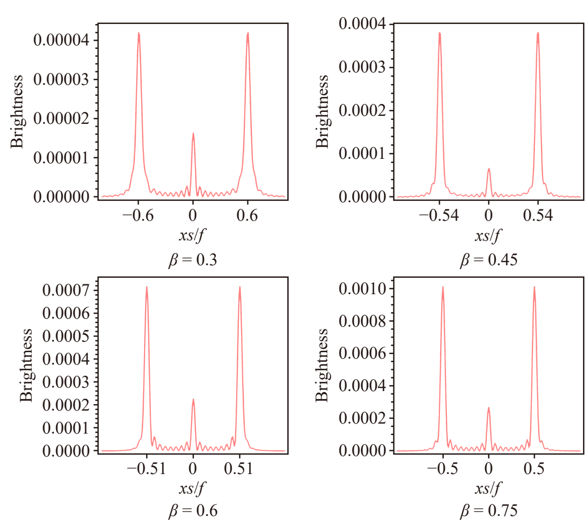

Fig. 11 Effect of β on the brightness, where $\theta_{obs} = 0$, $y_h = 5$, $\omega = 90$.

$$\cos\theta_{in} = \frac{g_{\alpha\beta}\upsilon^{\alpha}n^{\beta}}{|\upsilon|\,|n|}\,|_{r=\infty} = \sqrt{\frac{\dot{r}^2/G}{\dot{r}^2/G + \tilde{L}/r^2}}\,|_{r=\infty}, \quad (22)$$

further simplification leads to

$$\sin\theta_{in}^2 = 1 - \cos\theta_{in}^2 = \frac{\tilde{L}^2 z(r)}{\dot{r}^2 + \tilde{L}^2 z(r)}\,|_{r=\infty} = \frac{\tilde{L}^2}{\omega^2}. \quad (23)$$

When the two endpoints of a geodesic are aligned with the center of the BH, due to axial symmetry [31], an observer will perceive a ring-shaped image with a radius that corresponds to the incident angle θ_{in}. As a photon reaches the location of the photon sphere, it neither escapes nor falls into the BH, but instead begins to orbit around it. At this point, the angular momentum is denoted by L, and the equation of orbital motion for the photon at the photon ring is determined by the following conditions [30, 31, 33]:

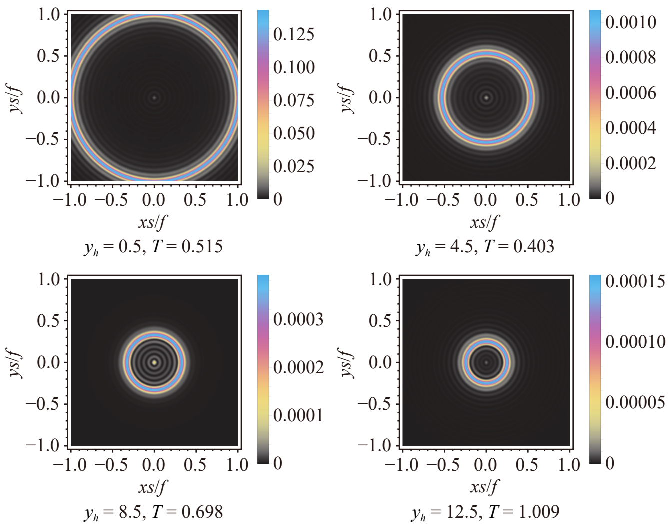

Fig. 12 Effect of T on the Einstein ring, where $\theta_{obs} = 0$, $\beta = 1$, $\omega = 90$.

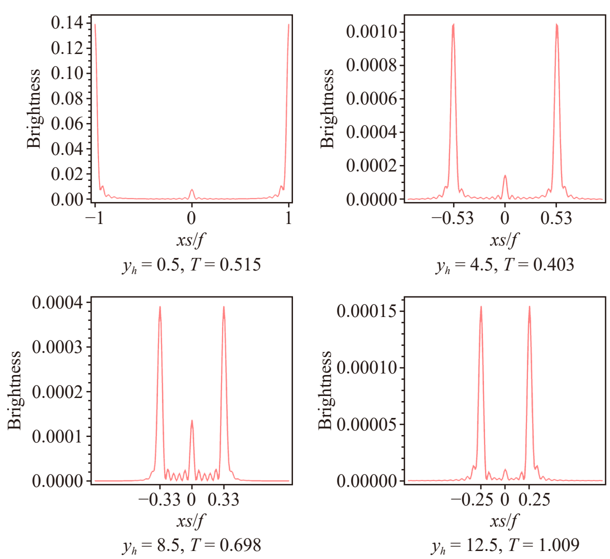

Fig. 13 Effect of T on the brightness, where $\theta_{obs} = 0$, $\beta = 1$, $\omega = 90$.

$$\dot{r} = 0, \mathrm{d}z/\mathrm{d}r = 0. \tag{24}$$

In the case, $\sin\theta_{in} = L/\omega$ is given, and from Fig. 14 $\sin\theta_R$ is observed to satisfy the relationship:

$$\sin\theta_R = r_R/f. \tag{25}$$

The incident angle of the photon and the angle of the photon ring both describe the angle of the photon ring that can be observed by an observer, and they should be essentially equal, that is

$$r_R/f = L/\omega. \tag{26}$$

When relevant physical parameters undergo changes, numerical methods are employed to verify the results

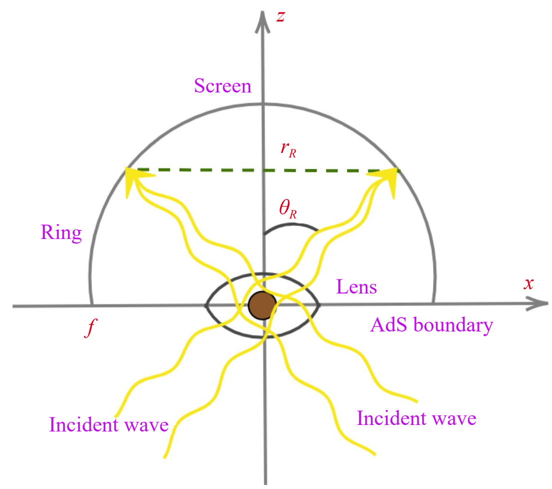

Fig. 14 Relation between ring radius r_R and ring angle θ_R.

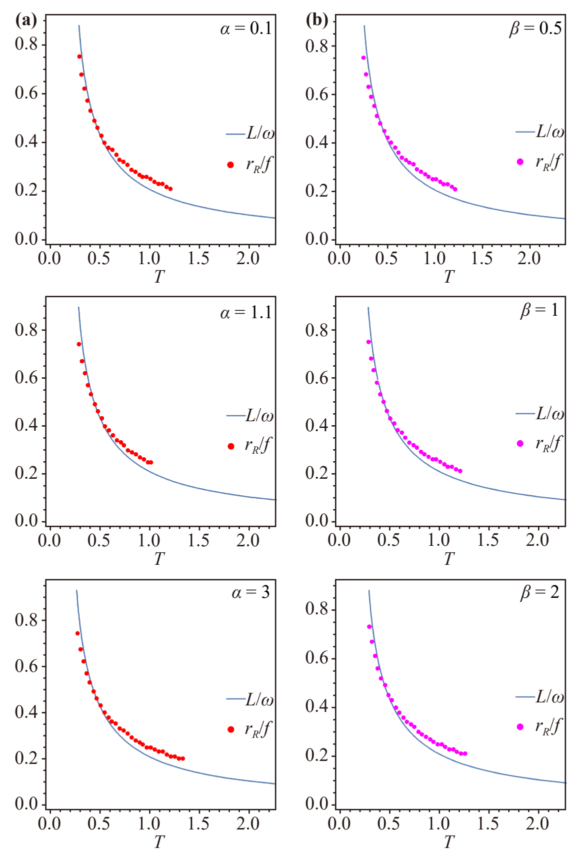

Fig. 15 **(a)** Comparing the Einstein ring radius between the geometric optics and wave optics for different values of α with $\omega = 90$. Where the discrete red points represent the Einstein ring radius derived from wave optics, while the blue curve depicts the variation in the radius of the circular orbit as the temperature changes, which is based on geometric optics. **(b)** Comparing the Einstein ring radius between the geometric optics and wave optics for different values of β with $\omega = 90$. Where the discrete magenta points represent the Einstein ring radius derived from wave optics, while the blue curve depicts the variation in the radius of the circular orbit as the temperature changes, which is based on geometric optics.

obtained from Eq. (26). Figure 15(a) illustrates the radius of the Einstein ring for various values of parameter α, while Fig. 15(b) depicts the radius of the Einstein ring for different values of parameter β. it is evident that the observed angle of the Einstein ring, obtained by wave optics, closely approximates the incident angle of the photon ring, which is derived from geometric optics. Notably, this conclusion holds irrespective of the deformation parameter α and the control parameter β, despite their influence on the fitting accuracy. In other words, the Einstein ring can be constructed holographically via wave optics.

4 Summary and conclusions

Using wave optics, the Einstein rings of the deformed AdS-Schwarzschild BH were investigated, based on AdS/CFT correspondence. By solving the asymptotic behavior of the wave function near the boundary, one can obtain the response of a Gaussian wave source at the south pole, measured at the north pole. The results indicate that the response function is the diffraction pattern formed by the scalar waves emitted from the wave source after being scattered by the BH. When $\beta = 1$, the amplitude of the response function increases with the increase of the deformation parameter α, but the response function decreases with the increase of the wave source frequency ω, and varies significantly with temperature. Similarly, when $\alpha = 1$, the amplitude of the response function decreases with the increase of both the control parameter β and the wave source frequency ω. Moreover, the amplitude of the response function also varies with temperature.

An optical system featuring a convex lens was employed for observing the corresponding holographic images. The result showed that when the control parameter β is fixed, the radius of the holographic ring gradually increases with the increase of the deformation parameter α. Additionally, as the event horizon increases, the ring radius decreases. Moreover, as the wave source frequency increases, the image becomes clearer. On the contrary, the deformation parameter α is fixed, the radius of the Einstein ring gradually decreases with the increase of control parameter β. Similarly, as the horizon radius increases, the ring radius decreases. Also, as the wave source frequency increases, the ring image becomes clearer.

Under the framework of geometric optics, a further study was conducted on the incident angle of the photon ring. Theoretical analysis and numerical simulation revealed that this result is consistent with the observation angle of the Einstein ring obtained through wave optics. This conclusion does not depend on deformation parameter α and control parameter β, although the α and β affect the fitting accuracy.

Declarations The authors declare that they have no competing interests and there are no conflicts.

Acknowledgements This work was supported by the National Natural Science Foundation of China (Grant Nos. 11675140, 11705005, and 12375043), the Innovation and Development Joint Foundation of Chongqing Natural Science Foundation (Grant No. CSTB2022NSCQ-LZX0021), and the Basic Research Project of Science and Technology Committee of Chongqing (Grant No. CSTB2023NSCQMSX0324).

References

1. J. M. Maldacena, The large N limit of superconformal field theories and supergravity, *Adv. Theor. Math. Phys.* 2(2), 231 (1998)
2. M. Natsuume, AdS/CFT duality user guide, *Lect. Notes Phys.* 903, 1 (2015)
3. S. A. Hartnoll, C. P. Herzog and G. T. Horowitz, Holographic superconductors, *J. High Energy Phys.* 12 (2008), 015
4. S. A. Hartnoll, C. P. Herzog, and G. T. Horowitz, Building a holographic superconductor, *Phys. Rev. Lett.* 101(3), 031601 (2008)
5. S. S. Gubser, Breaking an Abelian gauge symmetry near a black hole horizon, *Phys. Rev. D* 78(6), 065034 (2008)
6. M. Čubrović, J. Zaanen, and K. Schalm, String theory, quantum phase transitions, and the emergent Fermi liquid, *Science* 325(5939), 439 (2009)
7. H. Liu, J. McGreevy, and D. Vegh, Non-Fermi liquids from holography, *Phys. Rev. D* 83(6), 065029 (2011)
8. T. Faulkner, H. Liu, J. McGreevy, and D. Vegh, Emergent quantum criticality, Fermi surfaces, and AdS_2, *Phys. Rev. D* 83(12), 125002 (2011)
9. S. A. Hartnoll, J. Polchinski, E. Silverstein, and D. Tong, Towards strange metallic holography, *J. High Energy Phys.* 2010(4), 120 (2010)
10. S. S. Pal, Model building in AdS/CMT: DC conductivity and Hall angle, *Phys. Rev. D* 84(12), 126009 (2011)
11. B. S. Kim, E. Kiritsis, and C. Panagopoulos, Holographic quantum criticality and strange metal transport, *New J. Phys.* 14(4), 043045 (2012)
12. E. Mefford and G. T. Horowitz, Simple holographic insulator, *Phys. Rev. D* 90(8), 084042 (2014)
13. E. Kiritsis and J. Ren, On holographic insulators and supersolids, *J. High Energy Phys.* 2015(9), 168 (2015)
14. A. Donos and J. P. Gauntlett, Novel metals and insulators from holography, *J. High Energy Phys.* 2014, 7 (2014)
15. K. Akiyama, et al. [Event Horizon Telescope], First M87 event horizon telescope results. I. The shadow of the supermassive black hole, *Astrophys. J. Lett.* 875(1), L1 (2019)
16. K. Akiyama, et al. [Event Horizon Telescope], First Sagittarius A* event horizon telescope results. I. The shadow of the supermassive black hole in the center of the Milky Way, *Astrophys. J. Lett.* 930 (2022), L12
17. J. Shipley and S. R. Dolan, Binary black hole shadows, chaotic scattering and the Cantor set, *Class. Quantum Gravity* 33(17), 175001 (2016)
18. C. Bambi and K. Freese, Apparent shape of super-spinning

black holes, *Phys. Rev. D* 79(4), 043002 (2009)
19. F. Atamurotov, A. Abdujabbarov, and B. Ahmedov, Shadow of rotating Hořava–Lifshitz black hole, *Astrophys. Space Sci.* 348(1), 179 (2013)
20. K. J. He, J. T. Yao, X. Zhang, and X. Li, Shadows and photon motions in the axially symmetric Finslerian extension of a Schwarzschild black hole, *Phys. Rev. D* 109(6), 064049 (2024)
21. K. J. He, S. C. Tan, and G. P. Li, Influence of torsion charge on shadow and observation signature of black hole surrounded by various profiles of accretions, *Eur. Phys. J. C* 82(1), 81 (2022)
22. K. J. He, S. Guo, S. C. Tan, and G. P. Li, Shadow images and observed luminosity of the Bardeen black hole surrounded by different accretions, *Chin. Phys. C* 46(8), 085106 (2022)
23. G. P. Li and K. J. He, Observational appearances of a $f(R)$ global monopole black hole illuminated by various accretions, *Eur. Phys. J. C* 81(11), 1018 (2021)
24. K. J. He, X. Zhang, and X. Li, Shadows and observation intensity of black holes in the Randall–Sundrum brane world model, *Chin. Phys. C* 46(7), 075103 (2022)
25. A. K. Mishra, S. Chakraborty, and S. Sarkar, Understanding photon sphere and black hole shadow in dynamically evolving spacetimes, *Phys. Rev. D* 99(10), 104080 (2019)
26. P. G. Nedkova, V. K. Tinchev, and S. S. Yazadjiev, Shadow of a rotating traversable wormhole, *Phys. Rev. D* 88(12), 124019 (2013)
27. Y. X. Chen, H. B. Zheng, K. J. He, G. P. Li, and Q. Q. Jiang, Additional observational features of the thin-shell wormhole by considering quantum corrections, *Chin. Phys. C* 48(12), 125104 (2024)
28. K. J. He, Z. Luo, S. Guo, and G. P. Li, Observational appearance and extra photon rings of an asymmetric thin-shell wormhole with a Bardeen profile, *Chin. Phys. C* 48(6), 065105 (2024)
29. R. Shaikh, P. Kocherlakota, R. Narayan, and P. S. Joshi, Shadows of spherically symmetric black holes and naked singularities, *Mon. Not. R. Astron. Soc.* 482(1), 52 (2019)
30. K. Hashimoto, S. Kinoshita, and K. Murata, Einstein rings in holography, *Phys. Rev. Lett.* 123(3), 031602 (2019)
31. K. Hashimoto, S. Kinoshita, and K. Murata, Imaging black holes through the AdS/CFT correspondence, *Phys. Rev. D* 101(6), 066018 (2020)
32. Y. Kaku, K. Murata, and J. Tsujimura, Observing black holes through superconductors, *J. High Energy Phys.* 09(9), 138 (2021)
33. Y. Liu, Q. Chen, X. X. Zeng, H. Zhang, and W. Zhang, Holographic Einstein ring of a charged AdS black hole, *J. High Energy Phys.* 2022(10), 189 (2022)
34. X. X. Zeng, K. J. He, J. Pu, G. Li, and Q. Q. Jiang, Holographic Einstein rings of a Gauss–Bonnet AdS black hole, *Eur. Phys. J. C* 83(10), 897 (2023)
35. X. X. Zeng, L. F. Li, and P. Xu, Holographic Einstein rings of a black hole with a global monopole, *Eur. Phys. J. C* 84(7), 714 (2024)
36. X. X. Zeng, M. I. Aslam, R. Saleem, and X. Y. Hu, Holographic Einstein rings of black holes in scalar-tensor-vector gravity, arXiv: 2311.04680 [gr-qc] (2023)
37. X. Y. Hu, X. X. Zeng, L. F. Li, and P. Xu, Holographic study on Einstein ring for a charged black hole in conformal gravity, *Results Phys.* 61, 107707 (2024)
38. G. P. Li, K. J. He, X. Y. Hu, and Q. Q. Jiang, Holographic images of an AdS black hole within the framework of $f(R)$ gravity theory, *Front. Phys. (Beijing)* 19(5), 54202 (2024)
39. K. J. He, Y. W. Han, and G. P. Li, Holographic image features of Hayward-AdS black hole surrounded by quintessence dark energy, *Phys. Dark Univ.* 44, 101468 (2024)
40. Z. Luo, K. J. He, and J. Li, Holographic Einstein rings of AdS black holes in Horndeski theory, arXiv: 2409.11885 [gr-qc] (2024)
41. X. X. Zeng, L. F. Li, P. Li, B. Liang, and P. Xu, Holographic images of a charged black hole in Lorentz symmetry breaking massive gravity, *Sci. China Phys. Mech. Astron.* 68(2), 220412 (2025)
42. A. S. Khan and F. Ali, The dynamics of particles around time conformal AdS-Schwarzschild black hole, *Phys. Dark Univ.* 26, 100389 (2019)
43. L. G. C. Gentile, P. A. Grassi and A. Mezzalira, Introduction to Khovanov homologies I. Unreduced Jones superpolynomial, *J. High Energy Phys.* 2013, 65 (2013)
44. J. Dunn and C. Warnick, The Klein–Gordon equation on the toric AdS-Schwarzschild black hole, *Class. Quantum Gravity* 33(12), 125010 (2016)
45. T. K. Dey, Phase transition of AdS–Schwarzschild black hole and gauge theory dual in the presence of external string cloud, *Int. J. Mod. Phys. A* 33(33), 1850193 (2018)
46. N. Banerjee, A. Bhattacharjee and A. Mitra, Classical Soft Theorem in the AdS-Schwarzschild spacetime in small cosmological constant limit, *J. High Energy Phys.* 2021, 38 (2021)
47. M. R. Khosravipoor and M. Farhoudi, Thermodynamics of deformed AdS-Schwarzschild black hole, *Eur. Phys. J. C* 83(11), 1045 (2023)
48. I. R. Klebanov and E. Witten, Ads/CFT correspondence and symmetry breaking, *Nucl. Phys. B* 556(1–2), 89 (1999)